Hamiltonian Inference from Dynamical Excitations in Confined Quantum Magnets

Netta Karjalainen,[1,2,†] Zina Lippo,[2,3,†] Guangze Chen,[2,4] Rouven Koch,[2] Adolfo O. Fumega,[2] and Jose L. Lado[2,*]

[1] *Department of Chemistry, University of Helsinki, FI-00014 Helsinki, Finland*
[2] *Department of Applied Physics, Aalto University, FI-02150 Espoo, Finland*
[3] *Department of Physics, University of Helsinki, FI-00014 Helsinki, Finland*
[4] *Department of Microtechnology and Nanoscience, Chalmers University of Technology, 41296 Gothenburg, Sweden*

(Received 1 March 2023; revised 3 July 2023; accepted 25 July 2023; published 22 August 2023)

Quantum-disordered models provide a versatile platform to explore the emergence of quantum excitations in many-body systems. The engineering of spin models at the atomic scale with scanning tunneling microscopy and the local imaging of excitations with electrically driven spin resonance has risen as a powerful strategy to image spin excitations in finite quantum spin systems. Here, focusing on $S = 1/2$ lattices as realized by Ti in MgO, we show that dynamical spin excitations provide a robust strategy to infer the nature of the underlying Hamiltonian. We show that finite-size interference of the dynamical many-body spin excitations of a generalized long-range Heisenberg model allows the underlying spin couplings to be inferred. We show that the spatial distribution of local spin excitations in Ti islands and ladders directly correlates with the underlying ground state in the thermodynamic limit. Using a supervised-learning algorithm, we demonstrate that the different parameters of the Hamiltonian can be extracted by providing the spatially dependent and frequency-dependent local excitations that can be directly measured by electrically driven spin resonance with scanning tunneling microscopy. Our results put forward local dynamical excitations in confined quantum spin models as versatile witnesses of the underlying ground state, providing an experimentally robust strategy for Hamiltonian inference in complex real spin models.

DOI: 10.1103/PhysRevApplied.20.024054

I. INTRODUCTION

The engineering of entangled states of matter is one of the most-powerful strategies for designing exotic quantum materials. A paradigmatic example is the case of quantum-disordered ground states, generically emerging in quantum spin models, many-body ground states featuring long-range entanglement, and fractional excitations [1]. Besides a variety of bulk materials hosting potential quantum-spin-liquid ground states [2–6], an alternative strategy to design these states relies on bottom-up assembly atom by atom [7,8]. This strategy has been systematically exploited with scanning tunneling microscopy (STM), with which artificial spin lattices have been assembled with atomic precision [9–14]. Excitations in these artificial lattices can be measured with inelastic spectroscopy [15–17] and via electrically driven paramagnetic resonance [8,18–22]. These techniques allow the probing of the spin excitations locally in space, in contrast with neutron-scattering methods used in bulk materials [3]. However, systematic methods for inferring the ground state and microscopic description of a spin system from experimentally available data remain an open problem in quantum materials.

The bottom-up design of quantum spin lattices presents unique opportunities to understand the buildup of quantum-disordered states [1,7]. In particular, the spatial resolution of STM techniques allows the direct inference of the impact of finite-size effects on many-body excitations of quantum spin models [7,8]. From the experimental point of view, excitations in confined models provide the opportunity of inferring the Hamiltonian of the underlying system by exploitation of finite-size effects [23–25]. While this strategy has been widely demonstrated in electronic systems [23,26–34], spin systems are a much bigger, remarkable challenge due to the complex many-body nature of the ground states. Parameters from a Hamiltonian can be extracted in simple cases explicitly [8], yet quantum spin models with multiple parameters require more-powerful strategies [35]. Machine-learning-powered Hamiltonian learning has arisen as an effective strategy to infer descriptions of complex systems [36–41]. However,

*jose.lado@aalto.fi
†These authors contributed equally.

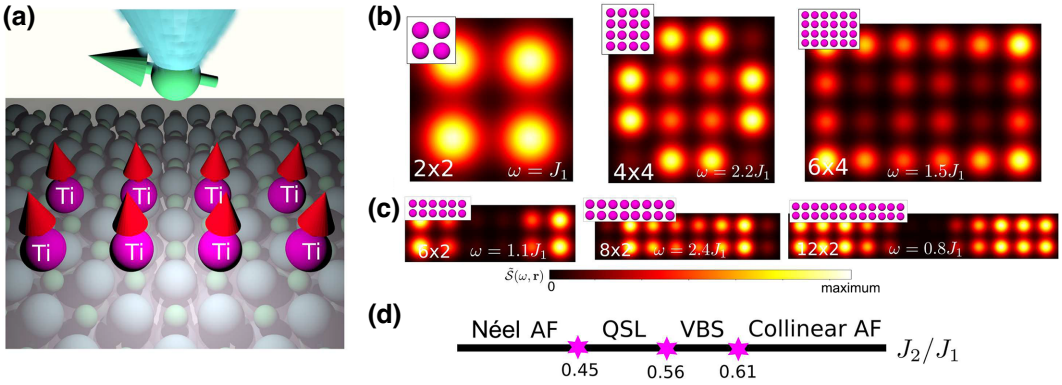

FIG. 1. (a) Artificial spin island of Ti in MgO whose magnetic excitations are measured with ESR-STM. (b),(c) Spatial distribution of spin excitations in different spin islands at frequencies $\omega = J_1$ for a 2×2 lattice, $\omega = 2.2J_1$ for a 4×4 lattice, $\omega = 1.5J_1$ for a 4×6 lattice, $\omega = 1.1J_1$ for a 6×2 lattice, $\omega = 2.4J_1$ for an 8×2 lattice, and $\omega = 0.8J_1$ for a 12×2 lattice. (b) Quasi-2D lattices of size 2×2, 4×4, and 6×4. (c) Quasi-1D lattices of size 6×2, 8×2, and 12×2. (d) Magnetic phase diagram realized by the frustrated spin Hamiltonian in the thermodynamic limit of a square lattice [Eq. (1)]. AF, antiferromagnetic; QSL, quantum spin liquid; VBS, valence bond state.

their potential for inferring the nature of frustrated quantum spin models from experimentally accessible spatially resolved and frequency-resolved excitations has not been demonstrated.

In this article, we show that excitations in finite quantum spin lattices provide a promising strategy to infer the underlying physics of the spin Hamiltonian by exploiting interference from finite-size effects. In particular, we show that a phase transition in the thermodynamic limit has a dramatic impact on the spatial distribution of the many-body modes of finite quantum spin islands, both in the presence and in the absence of magnetic fields. Furthermore, we demonstrate that this strong dependence allows the development of a strategy to learn the Hamiltonian parameters of the spin model directly from the spatially dependent and frequency-dependent excitations, accessible with direct experimental measurements. Our results demonstrate that finite-size effects provide a valuable strategy for Hamiltonian learning of quantum spin models.

II. MAGNETIC PHASES IN A CONFINED QUANTUM MAGNET

In the following, we focus on the spin model realized by Ti atoms on MgO [8,21,42,43], which was recently demonstrated to realize spin excitations in 2×2 lattices [8]. Figure 1(a) shows a schematic of the experimental procedure based on STM and single-atom electron spin resonance (ESR) used to probe these artificial spin islands and to measure their spin excitations. Different island geometries with various sizes are illustrated in Figs. 1(b) and 1(c), showing the appearance of a spatial pattern in the spin excitations at specific energies. This pattern in the spin excitation constitutes the fundamental idea for our analysis.

The associated spin Hamiltonian that describes these spin islands takes the form

$$\mathcal{H} = J_1 \sum_{\langle \mathbf{r}_i, \mathbf{r}_j \rangle} \mathbf{S}_{\mathbf{r}_i} \cdot \mathbf{S}_{\mathbf{r}_j} + J_2 \sum_{\langle\langle \mathbf{r}_i, \mathbf{r}_j \rangle\rangle} \mathbf{S}_{\mathbf{r}_i} \cdot \mathbf{S}_{\mathbf{r}_j}, \qquad (1)$$

where J_1 and J_2 are the nearest and next-nearest antiferromagnetic spin exchanges; for simplicity, we take $J_1 = 1$ [44]. In the thermodynamic limit, this frustrated Hamiltonian develops different magnetic phases depending on the J_2/J_1 ratio [45–49], including antiferromagnetic Néel, stripe, quantum-spin-liquid, and bond-ordered phases, as summarized in Fig. 1(d). The antiferromagnetic interactions leading to these phases are the ones that appear in Ti due to superexchange. For Ti in MgO, the couplings J_1 and J_2 are controlled by the distance between Ti and the thickness of MgO layers. It is also worth noting that the thickness of MgO may have an impact on the J_1, J_2, and J_3 due to the contribution to the exchange mediated by the underlying silver substrate in experiments. The impact of silver on the magnetic properties of Ti and other $3d$ atoms was addressed previously [50–53], demonstrating the notable role of the MgO substrate in modifying the effective spin Hamiltonian.

The physical quantity that we use to characterize the magnetic phase in the confined quantum magnets is the spin dynamical correlator $\mathcal{S}(\omega, \mathbf{r}_i)$, defined as

$$\mathcal{S}(\omega, \mathbf{r}_i) = \langle \mathrm{GS} | S^z_{\mathbf{r}_i} \delta(\omega + E_{\mathrm{GS}} - \mathcal{H}) S^z_{\mathbf{r}_i} | \mathrm{GS} \rangle, \qquad (2)$$

where $|\mathrm{GS}\rangle$ and E_{GS} are the many-body ground state and its energy [54–56]. The parameter ω accounts for the frequency of the excitation, which in ESR experiments corresponds to the frequency of the applied voltage. It is worth noting that the line shape of the ESR can be different from the dynamical spin correlator, yet the frequencies

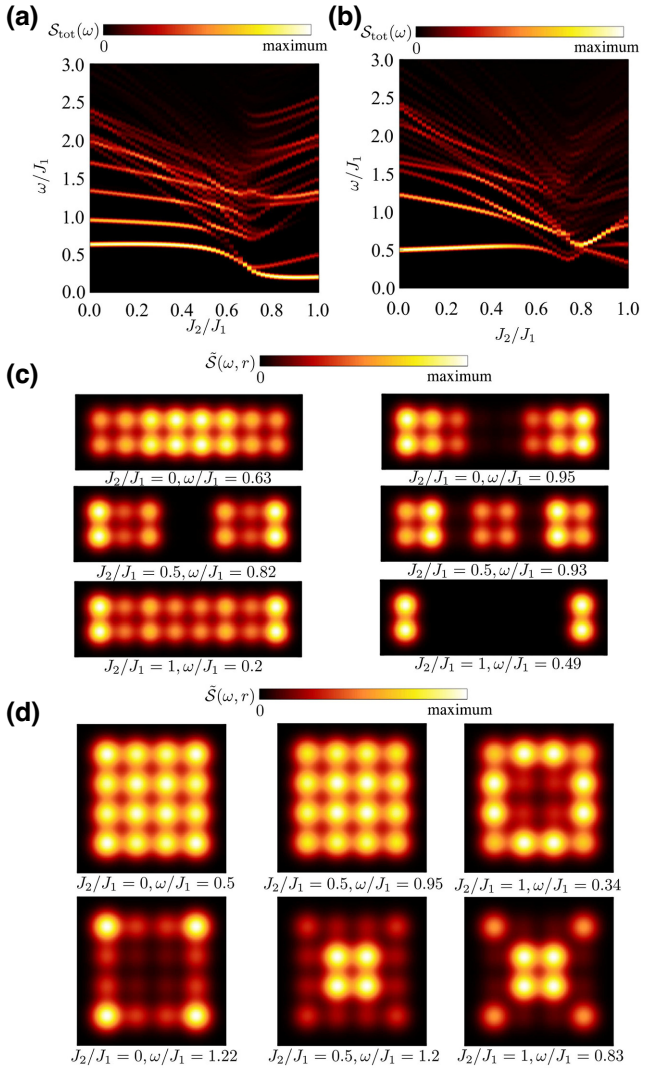

FIG. 2. Total spin spectral function in (a) an 8×2 ladder and (b) a 4×4 ladder as a function of J_2. (c) Local spectral function at different energies ω and J_2 for the 8×2 ladder. (d) Local spectral function at different energies ω and J_2 for the 4×4 ladder. It is observed that both in the ladder and in the island the confined modes depend on the energy ω and the second-neighbor coupling J_2.

at which the features appear will be the same for both quantities. Equation (2) characterizes local spin excitations, which directly influence inelastic-electron-tunneling spectroscopy and electron paramagnetic resonance [17,50,57,58]. It is worth noting that in both inelastic-electron-tunneling spectroscopy and electron paramagnetic resonance, additional form factors stemming from transport can slightly modify the signal in comparison with the pure spin spectral function [59].

For concreteness, we focus on the dynamical spin correlator for two different geometries: a quasi-1D 8×2 ladder and a quasi-2D 4×4 dot. The spin systems are the most-realistic ones that may be assembled from the already-demonstrated structures, which achieved an engineered 2×2 cluster [8]. Figure 2 shows the total dynamical correlator $S_{\rm tot}(\omega) = \sum_{\mathbf{r}_i} S(\omega, \mathbf{r}_i)$ and the local correlator for different regimes of J_2/J_1 of the spin Hamiltonian. The total correlator [Figs. 2(a) and 2(c)] shows a clear dependence on J_2/J_1, thus providing a hint as to where in the phase diagram the system is. In Figs. 2(b) and 2(d), we can observe the strong spatial dependence of the local spin correlator $\mathcal{S}(\omega, \mathbf{r}_i)$ for different J_2/J_1 values. This dramatic difference suggests that the change of the confined many-body spin excitations can provide a useful strategy to infer the form of the underlying spin Hamiltonian and determine the regime of the phase diagram in which the system is.

We can analyze in a more-systematic way the evolution of the local spin correlator as a function of J_2/J_1 for the different inequivalent sites of the islands that we are studying. Figures 3(a)–3(d) show results for the 8×2 ladder, and Figs. 4(a)–4(c) show results for the 4×4 island. Moreover, to reveal the potential phase transitions more clearly, we consider adding a staggered antiferromagnetic field $B_{\rm AF}$ [Figs. 3(e)–3(h) and 4(d)–4(f)] and a striped antiferromagnetic field $B_{\rm SAF}$ [Figs. 3(i)–3(l) and 4(g)–4(i)] to the Hamiltonian in Eq. (1) and study the changes that they produce to the local dynamical correlators. We start by analyzing the cases without an external local Zeeman field [Figs. 3(a)–3(d) and 4(a)–4(c)]. In all cases, the dynamical correlator shows several peaks at $J_2/J_1 = 0$. As J_2/J_1 increases, the peaks at higher energy move toward zero energy. Eventually, at around $J_2/J_1 = 0.8$, these peaks merge, and then they disperse for larger J_2/J_1.

Interestingly, the nanoscale nature of these magnets allows the engineering of local fields by depositing atoms atoms realizing a strong Ising spin close to the spin-lattice, as is the case of Ho at MgO [18] or Dy at MgO [60]. These Ising spins allow the creation of local Zeeman fields in nearby spins and can be controlled individually, allowing one to engineer atomically precise Zeeman profiles [60]. Atomically engineered Zeeman fields provide a strategy to probe the response of a quantum magnet to different Zeeman textures and, in particular, to distinguish between different states depending on their response. Using the previous idea, in the following, we include a local Zeeman term that will be induced by proximal Ising spins as

$$\mathcal{H}_Z = \sum_{\mathbf{r}_i} \mathbf{B}_{\mathbf{r}_i} \cdot \mathbf{S}_{\mathbf{r}_i}, \tag{3}$$

where $\mathbf{B}_{\mathbf{r}_i}$ is the local Zeeman field created by proximal Ising spins. We note that while a Zeeman profile for the quasi-1D structures in Fig. 1(c) can be engineered in all the sites, Zeeman profiles in the quasi-2D structures in Fig. 1(b) would be more challenging. As a reference, we illustrate the impact of those profiles for quasi-1D and quasi-2D cases, keeping in mind that the quasi-1D cases will be experimentally easier to implement. We

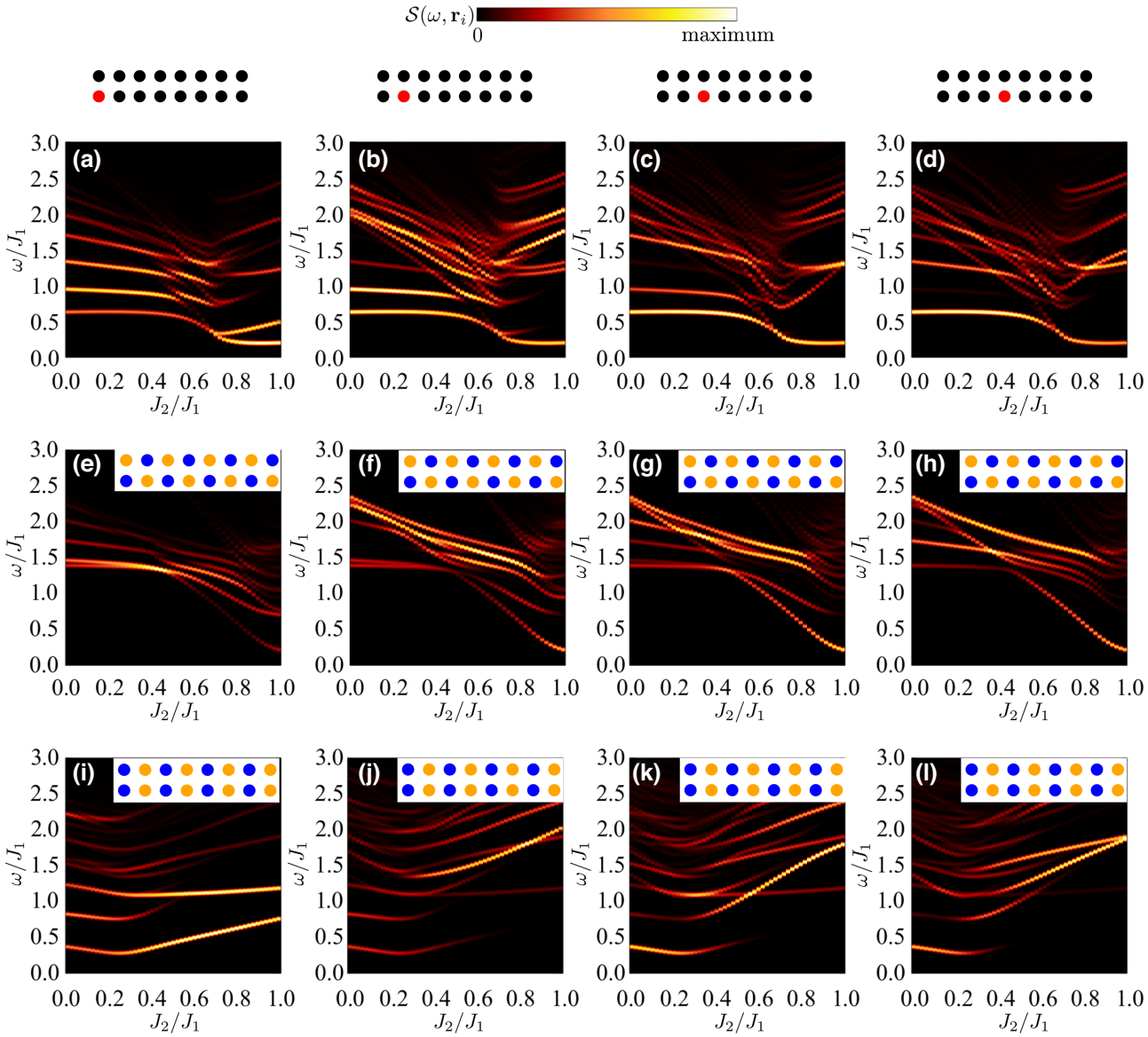

FIG. 3. Local spectral function at different energies ω and J_2/J_1 on different inequivalent sites for the 8×2 ladder, with (a)–(d) no magnetic field, (e)–(h) $B_{\mathrm{AF}} = 0.5$, and (i)–(l) $B_{\mathrm{SAF}} = 0.5$. The insets in (e)–(l) show the local magnetic fields $B_i = 0.5J_1$ and $B_i = -0.5J_1$ on an orange site and a blue site, respectively.

address specific Zeeman profiles, staggered antiferromagnetic and collinear antiferromagnetic, that promote the two symmetry-broken states shown in Fig. 1(d). The cases with the staggered antiferromagnetic field B_{AF} [Figs. 3(e)–3(h) and 4(d)–4(f)] show a drastic change of the spectrum for $0 < J_2/J_1 < 0.6$: the lowest excitation, at around $\omega = 0.5J_1$, vanishes. When $J_2/J_1 > 0.6$, the change is less significant: the levels are shifted, but there is no vanishing of strong peaks. This suggests that for $J_2/J_1 < 0.6$ the ground state has a large staggered antiferromagnetic component as it is sensitive to a staggered antiferromagnetic field, while for $J_2/J_1 > 0.6$ the ground state does not have a large staggered antiferromagnetic component. Similarly, we can analyze the dynamical correlators in the presence of a striped antiferromagnetic field B_{SAF} [Figs. 3(i)–3(l) and 4(g)–3(i)]: for $J_2/J_1 < 0.4$, the spectrum does not change very much, while for $J_2/J_1 > 0.4$ the lowest states vanish. This indicates a large striped antiferromagnetic component in the ground state for $J_2 > 0.4$. This phenomenology reflects the behavior of the state in the thermodynamic limit [61]. For $J_2/J_1 < 0.4$, the ground state is almost-staggered antiferromagnetic, while for $J_2/J_1 > 0.6$, the ground state is almost a striped antiferromagnetic, and for $0.4 < J_2/J_1 < 0.6$, the ground state is in a frustrated

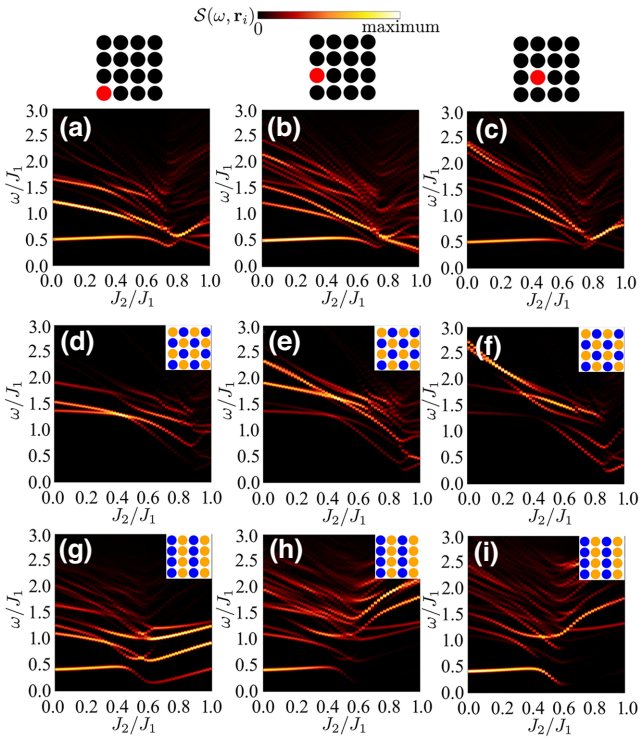

FIG. 4. Local spectral function at different energies ω and J_2 on different sites for the 4×4 island, with (a)–(d) no magnetic field, (e)–(h) $B_{\mathrm{AF}} = 0.5$, and (i)–(l) $B_{\mathrm{SAF}} = 0.5$. The insets in (d)–(i) show the local magnetic fields $B_i = 0.5J_1$ and $B_i = -0.5J_1$ on an orange site and a blue site, respectively.

regime having competing staggered-antiferromagnetic and striped-antiferromagnetic components.

The above analysis demonstrates three different phases in the 8×2 ladder and the 4×4 island as a function of J_2/J_1. Furthermore, it shows that the dependence of the spin excitations on a local field changes dramatically depending on the value of J_2/J_1. This severe change of dynamical excitations with a local field directly reflects the nature of the different ground states as a function of J_2/J_1. Despite our having determined the connection between the local dynamical spin excitations and the different phases realized by the spin Hamiltonian, there are some limitations that must be overcome to accurately infer the form of the Hamiltonian, i.e., the precise J_2/J_1 ratio from the local spin dynamical correlator that one would measure in an experiment. In particular, we have been using a local magnetic field to analyze the evolution of the dynamical correlation with different antiferromagnetic external fields. While such local fields can be engineered in certain structures, as noted above [60], from an experimental point of view, uniform magnetic fields are easier to control externally. As we see below, even with a uniform magnetic field, the nature of the different ground states can be inferred from the local excitations by exploitation of the dependence on confinement interference effects. The thickness of MgO is expected to have an impact on J_1/J_2 due to the contribution to the exchange mediated by the underlying silver substrate in experiments. Specifically, thin MgO substrates will give rise to a substantial increase of J_2/J_1. In contrast, for large thicknesses of MgO, J_1 is expected to dominate due to exchange being dominated by superexchange through MgO. The impact of silver on the magnetic properties of Ti and other $3d$ atoms was addressed previously [50–53], demonstrating the notable role of the MgO substrate in modifying the effective spin Hamiltonian. The theoretical analysis above approximately established the different phase transitions from the evolution of the dynamical correlators. However, it would be better to provide a way to directly get the precise J_2/J_1 ratio from the correlator that would be directly measured in experiments. In the following section, we establish a protocol to systematically infer the specific form of the Hamiltonian from the dynamical correlator.

III. HAMILTONIAN LEARNING FROM CONFINED QUANTUM SPIN EXCITATIONS

In the previous section, we observed that the spatially resolved dynamical excitations show a distinct dependence on the Hamiltonian parameters. While extraction of the parameters from the data is a nontrivial task, machine-learning methods allow the data to be processed without the need for explicitly programmed and task-depended algorithms. The algorithm learns to solve the task and creates a model purely from data, thus overcoming the issues that we have described.

In the following we report the use of supervised learning with neural networks (NNs). NNs are used to perform a regression task, which assumes a relationship between the inputs and outputs of the model. Here, the inputs are (local) dynamical correlators [given by Eq. (2)] and the outputs are the corresponding exchange parameters of the Hamiltonian. A sketch of the workflow of the NN is shown in Fig. 5(a).

The NN acts as a universal function approximator, finding a function f, mapping from the inputs X to the outputs y. By optimization of the NN parameter, we obtain $y = f(X)$. For the optimization task we use supervised learning and a gradient-decent algorithm, i.e., teaching the NN by showing examples of pairs of inputs and outputs to minimize the loss function and update the NN parameter (weights). The input of the NN contains the map of dynamical correlators at the difference frequencies. By using the symmetry of the lattices, we reduce the whole map to three (four) independent dynamical correlators of the 4×4 (8×2) system in combination with an external uniform magnetic field, which is easier to implement in experiments. This results in a total dimension of 601 (801). The NN architecture consists of three hidden layers of dimensions 200, 200, and 100 and an output dimension of 2. We

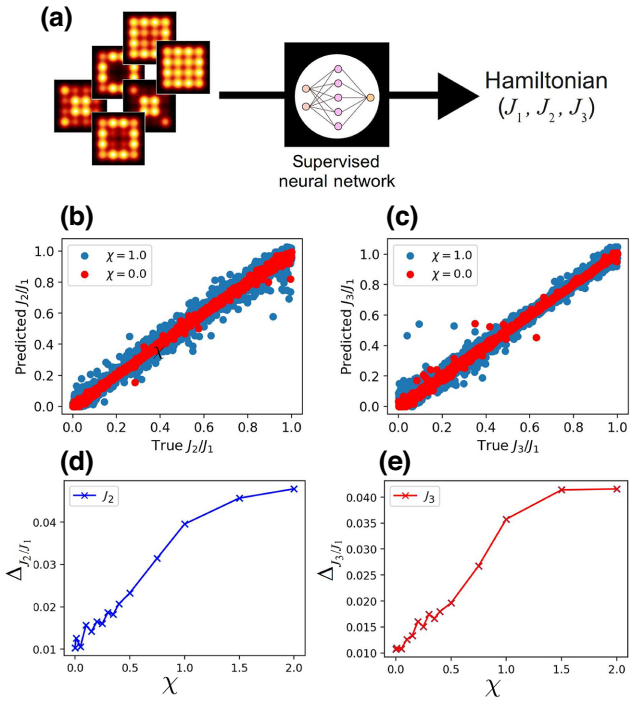

FIG. 5. (a) Schematic workflow of the NN, taking dynamical correlators as input and returning the underlying Hamiltonian parameter (J_1, J_2, J_3). (b)–(e) Results for the 2×8 lattice including the predictions versus the true values of (b) J_2 and (c) J_3 with noise ($\chi = 1$) and without noise. (d),(e) Corresponding mean error Δ_{J_2/J_1} and Δ_{J_3/J_1} for noise up to $\chi = 2$ for J_2 and J_3.

demonstrate our algorithm with a more-complex Heisenberg Hamiltonian, incorporating first-neighbor, second-neighbor, and third-neighbor exchange $(J_2/J_1, J_3/J_1)$ of the form

$$H = J_1 \sum_{\langle \mathbf{r}_i, \mathbf{r}_j \rangle} \mathbf{S}_{\mathbf{r}_i} \cdot \mathbf{S}_{\mathbf{r}_j} + J_2 \sum_{\langle\langle \mathbf{r}_i, \mathbf{r}_j \rangle\rangle} \mathbf{S}_{\mathbf{r}_i} \cdot \mathbf{S}_{\mathbf{r}_j} + J_3 \sum_{\langle\langle\langle \mathbf{r}_i, \mathbf{r}_j \rangle\rangle\rangle} \mathbf{S}_{\mathbf{r}_i} \cdot \mathbf{S}_{\mathbf{r}_j} + \mathbf{B} \cdot \sum_{\mathbf{r}_i} \mathbf{S}_{\mathbf{r}_i}, \quad (4)$$

where $\mathbf{B} = (B_x, 0, 0)$, and where we added third-neighbor interactions (J_3) as well as an external magnetic field with strength B_x. We set $J_1 = 1$ as the energy scale and we vary J_2, J_3, and B_x in the interval $I = [0, 1]$ to cover a wide range of the parameter space of the Hamiltonian. The magnetic field B_x is measured in the unit of $g\mu_B/J_1$, with $g = 1$ the Landé g factor and μ_B the Bohr magneton. We use the Hamiltonian parameters J_2 and J_3 as labels in the dataset to train the NN. The trained model is then able to predict the underlying exchange Hamiltonian parameters J_2 and J_3 by use of the dynamical correlators and the magnetic field strength as inputs. We train the NN for 100 epochs with a batch size of 10 to obtain the results shown in this work. We use this procedure to address the 2×8 and 4×4 lattices presented in the previous section. The general machine-learning workflow is shown in Fig. 5(a). The NN takes as input dynamical correlators with corresponding magnetic field B_x to predict the corresponding J_2 and J_3 interactions.

To demonstrate that NN Hamiltonian inference is a robust method to be applied to experimental data, we introduce noise in the dynamical correlators used to infer J_2 and J_3 interactions. Noise is included as a random frequency-dependent renormalization of the dynamical correlators defined as

$$\mathcal{S}(\omega, \mathbf{r}_i)_{\text{noisy}} = \mathcal{S}(\omega, \mathbf{r}_i) \cdot |1 + \zeta(\omega)|. \quad (5)$$

The noise $\zeta(\omega)$ is defined as a uniform distribution in the interval $\zeta(\omega) \in [-\chi, \chi]$, randomly sampled for each Hamiltonian, and is different for every discrete frequency of the dynamical correlators.

Figures 5(b)–5(e) show the results for the 2×8 lattice, starting with the predictions for J_2 and J_3 [in Figs. 5(b) and 5(c)] in the presence and in the absence of noise. The predictions are plotted against the true values, and in the ideal case, all data points lie exactly on the diagonal line [of $f(x) = x$]. Without the presence of noise (red), the NN predicts both values with very high precision, with mean error (ME) $\Delta_{J_2/J_1} = 0.0103$ and $\Delta_{J_3/J_1} = 0.0107$. However, even in the presence of very high noise levels ($\chi = 1$), the NN is able to make predictions with mean errors $\Delta_{J_2/J_1} = 0.040$ and $\Delta_{J_3/J_1} = 0.036$. This shows the high resilience to noise of our approach, which is an important factor when one is considering experimental data. The resilience to noise is highlighted even more in Figs. 5(d) and 5(e), where the mean square error is shown for different noise levels for J_2 and J_3. As seen in Figs. 5(d) and 5(e), the MSE stays very low up to a noise level χ of 0.5 added to the dynamical correlators, when it slowly starts increasing. Even for noise levels χ of 1 or greater, the errors remain relatively small. The NN is still able to make good predictions for noise levels χ of 1 or greater. For the following predictions, we use added noise with amplitude $\chi = 0.02$ since it can be beneficial for the training of the NN so as to avoid overfitting.

The same analysis is done for the 4×4 lattice in Fig. 6. In this case, we trained the network with dynamical correlators of the 4×4 system. The results are almost identical to those for the 2×8 lattice shown in Fig. 5. Figures 6(a) and 6(b) show the predictions versus the true Hamiltonian parameter for J_2 and J_3, respectively, which are of very high precision for no noise, and even up to noise amplitudes χ of 1, the NN predicts the parameters accurately. For both parameters without noise, $\Delta_{J_2/J_1} = 0.016$ and $\Delta_{J_3/J_1} = 0.016$, and with added noise of $\chi = 1$, the NN is again able to make predictions with low errors, $\Delta_{J_2/J_1} = 0.053$ and $\Delta_{J_3/J_1} = 0.042$. We also see similar behavior for the ME for different noise levels in Figs. 6(c) and 6(d). Also for this system the ME starts increasing

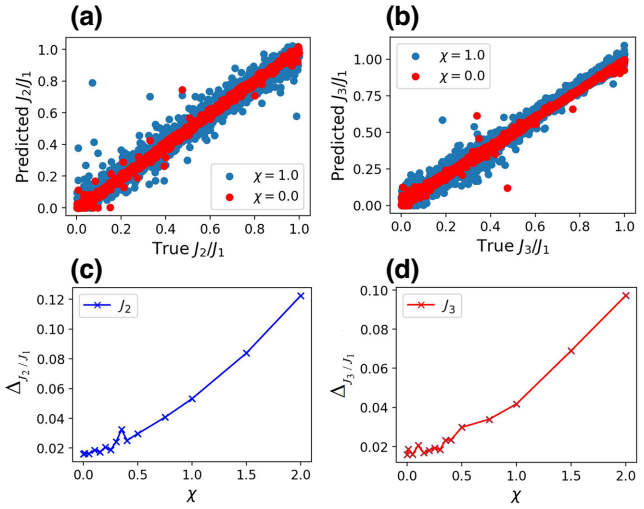

FIG. 6. (a)–(d) Results for the 4×4 lattice including the predictions versus true values of (a) J_2 and (b) J_3 with noise ($\chi = 1$) and without noise. (c),(d) Corresponding mean error of (c) J_2 and (d) J_3 for added noise up to $\chi = 2$.

from a noise amplitude χ of 1 but does not saturate at $\chi = 1.5$ as is the case for the 2×8 lattice. Nonetheless, the NN is very resilient to noise and able to make good predictions.

Figure 7 shows the predictions of the local spin correlation function made by the NN in comparison with numerical calculations for the 4×4 system in two different regions of the Hamiltonian. It is shown that the NN performs well for the antiferromagnetic phase Fig. 7(a)] as well as for the valence bond state phase [Fig. 7(b)]. The predictions are almost indistinguishable from the numerical calculations, including all significant features, and show only very minor deviations. The same results are obtained for the 2×8 ladder presented in Fig. 8 for the same Hamiltonian parameter, where the NN performs equally well in predicting the local spectral function for three different energies. The high precision of the NN predictions is related to the high accuracy in the predictions of the Hamiltonian parameter and the small mean error discussed before.

Finally, we discuss some additional considerations regarding the experimental parameter extraction in generic spin lattices beyond Ti in MgO. While for Ti in MgO, the spin excitations are dominated by the isotropic Heisenberg coupling model, in generic experimental realizations, there can be additional contributions to the Hamiltonian. In particular, a contribution to the spin coupling stemming from dipolar interaction can appear [62]. This contribution can be accurately computed from the geometry of the island. As a result, such a term can be explicitly included in the Hamiltonian, and its prefactor does not have to be inferred. In addition, small anisotropic exchange contributions coming from spin-orbit coupling can appear in real-spin models. While such a contribution is small for Ti lattices, lattices made of heavier $4d$ or $5d$ atoms can display stronger anisotropic exchange stemming from spin-orbit coupling [18]. In those instances, the anisotropic term should be included in the Hamiltonian, with a parameter that has to be inferred in the supervised learning. Furthermore, in the case of lattices with $S > 1/2$, such as Fe in MgO [58], local spin-anisotropy terms would have to be included in the Hamiltonian and inferred in the learning. Finally, if the Hamiltonian inference is made in the presence of a large external magnetic field, an anisotropic g factor may appear [63] and could become an additional parameter to be extracted. In Appendixes A and B, we

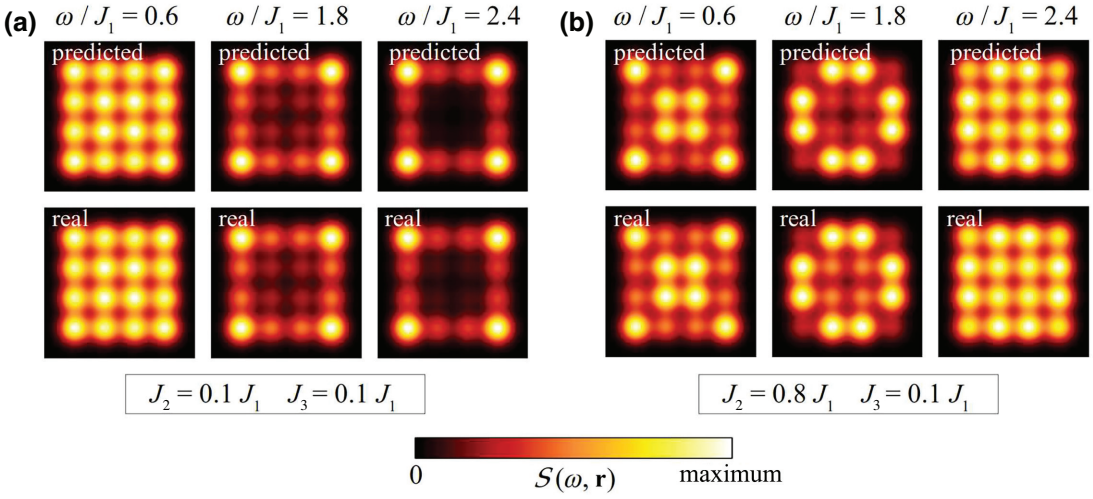

FIG. 7. Local spectral function at three different energies ω for the 4×4 system. Shown are the predictions of the NN (top) in comparison with numerical computations (bottom) for the Hamiltonians with (a) $J_2 = 0.1J_1$ and $J_3 = 0.1J_1$ ($B_x = 0$) and (b) $J_2 = 0.8J_1$ and $J_3 = 0.1J_1$ ($B_x = 0$).

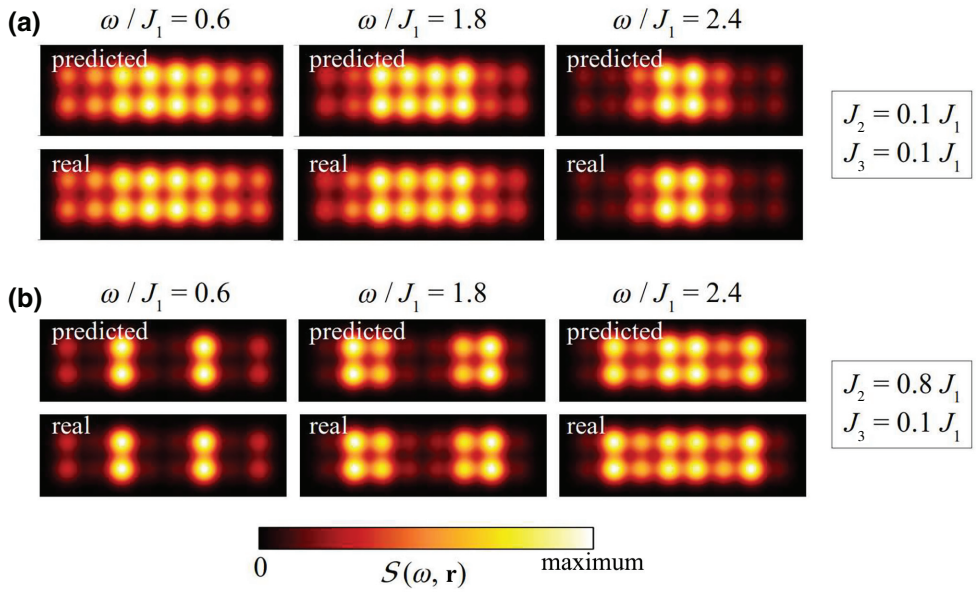

FIG. 8. Local spectral function at three different energies ω for the 2×8 ladder. Shown are the predictions of the NN (top) in comparison with numerical computations (bottom) for the Hamiltonians with (a) $J_2 = 0.1J_1$ and $J_3 = 0.1J_1$ ($B_x = 0$) and (b) $J_2 = 0.8J_1$ and $J_3 = 0.1J_1$ ($B_x = 0$).

show that the NN formalism can be extended to infer both the anisotropy strength and the g factor. This demonstrates the potential of machine-learning algorithms to infer generalized Hamiltonians with multiple parameters.

Finally, it is worth emphasizing the clear advantage of our algorithm with respect to conventional fitting procedures. Our machine-learning algorithm requires evaluation of the spin spectral function only to train the algorithm initially, a task that can be systematically parallelized. This means that once the algorithm is trained, parameters can be obtained instantly, extracted just by provision of the measured spectral function. In contrast, conventional fitting algorithms require iterative evaluation of the spin spectral function of the model for different parameters up to several hundred times, a task that can become time-consuming. This evaluation cannot be done in parallel, as each parameter chosen depends on the quality of the fitting for the previous one. This implies that our method provides a nearly instantaneous Hamiltonian extraction in comparison with the standard fitting method. This massive speedup is especially relevant for use of our algorithm with automated impurity assembly as recently demonstrated [64], as our method would allow one to estimate on the fly the Hamiltonian of each realized atomic arrangement.

IV. CONCLUSION

To summarize, we have shown that spatially resolved and frequency-resolved spin excitations in finite-size spin models allow inference of the underlying long-range frustrated Heisenberg Hamiltonian. Our method exploits the finite-size effects of a quantum spin island, demonstrating that confinement in the many-body spin modes provides a strategy to extract microscopic couplings. From the experimental point of view, our results show that spatial and frequency resolution of electrically driven spin resonance with scanning tunneling microscopy allows extraction of the nature of complex Hamiltonians from confinement effects in finite spin systems. In particular, by focusing on the $S = 1/2$ Heisenberg model as realized by Ti in MgO, we showed that the spatial distribution of spin excitations strongly depends on the underlying exchange couplings of the model. This strong dependence displayed in finite systems can be rationalized by the different nature of the ground state in the thermodynamic limit, which impacts the spin excitations even in small, confined islands. We demonstrated that such finite-size effects allow the development of a supervised-learning method for extraction of the parameters of the Hamiltonian from the full frequency and spatially resolved spin excitations. We showed that this method is robust with regard to noise in the dynamical spin excitations, establishing an experimentally realistic strategy for Hamiltonian inference using real data from paramagnetic resonance measurements with scanning tunneling microscopy. Our method allows confined excitations in frustrated magnets to be used as a powerful strategy to understand the buildup and nature of frustrated quantum spin many-body models.

ACKNOWLEDGMENTS

We acknowledge the computational resources provided by the Aalto Science-IT project, financial support from the Academy of Finland (Projects No. 331342, No. 336243,

and No. 349696), and the Jane and Aatos Erkko Foundation. We thank K. Yang, T. Kurten, P. Liljeroth, S. Kezilebieke, and R. Drost for useful discussions.

APPENDIX A: g-FACTOR PREDICTIONS

While in the main text we focused on predicting exchange constants, additional terms may appear in the Hamiltonian. Specifically, spin-orbit-coupling effects give rise to a renormalized g factor affecting the Zeeman term. We now show that our algorithm would be capable of predicting this additional term. Figure 9 shows the predictions for the g factor for the 2×8 lattice and the 4×4 lattice. We included the g factor in the Hamiltonian as

$$H = J_1 \sum_{\langle \mathbf{r}_i, \mathbf{r}_j \rangle} \mathbf{S}_{\mathbf{r}_i} \cdot \mathbf{S}_{\mathbf{r}_j} + J_2 \sum_{\langle\langle \mathbf{r}_i, \mathbf{r}_j \rangle\rangle} \mathbf{S}_{\mathbf{r}_i} \cdot \mathbf{S}_{\mathbf{r}_j} + J_3 \sum_{\langle\langle\langle \mathbf{r}_i, \mathbf{r}_j \rangle\rangle\rangle} \mathbf{S}_{\mathbf{r}_i} \cdot \mathbf{S}_{\mathbf{r}_j} + g\mathbf{B} \cdot \sum_{\mathbf{r}_i} \mathbf{S}_{\mathbf{r}_i}, \tag{A1}$$

where the Zeeman term is renormalized by the g factor g. The NN is trained to predict the g factor, chosen in the interval [0.2, 2.0]. These results show that our machine-learning algorithm is capable of predicting the g factor in addition to J_2 and J_3 with good accuracy.

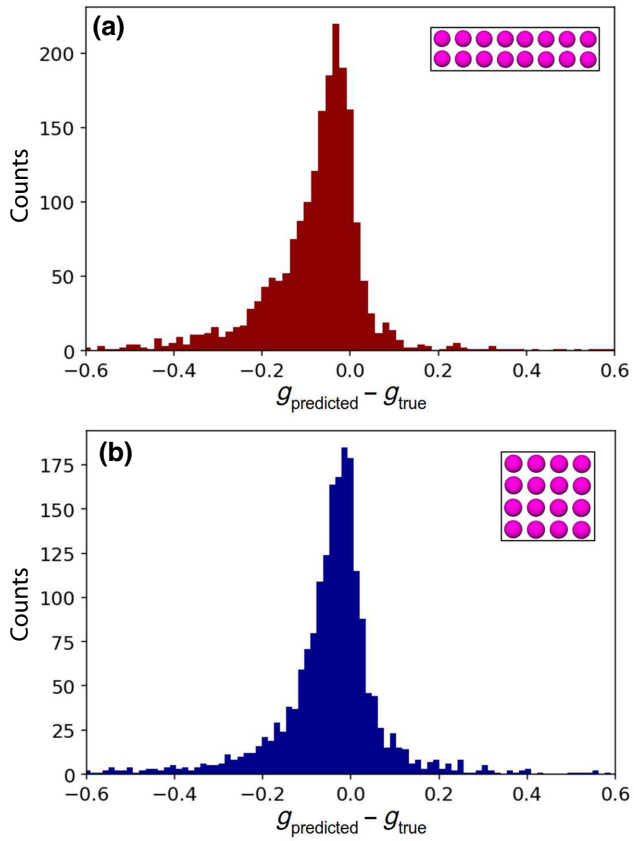

FIG. 9. Histogram of g-factor predictions for (a) the 2×8 lattice and (b) the 4×4 lattice. The number of counts is plotted against the difference between the prediction and the true value. For (a) the mean absolute error $\Delta = 0.101$ and for (b) $\Delta = 0.092$.

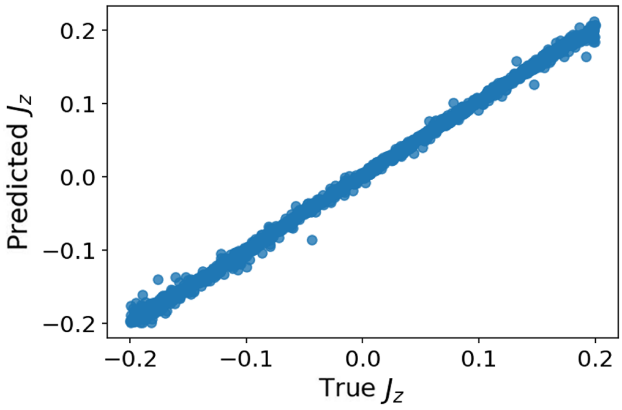

FIG. 10. Predicted anisotropy strength J_z versus true value for the 4×4 lattice. The mean absolute error $\Delta = 0.014$.

APPENDIX B: ANISOTROPIC EXCHANGE PREDICTIONS

An additional term that emerges in the spin Hamiltonian due to spin-orbit coupling is the anisotropic exchange term. In the following we show that our algorithm can be easily extended to extract anisotropic exchange interactions. Figure 10 shows the predictions for the anisotropy first-neighbor exchange correction J_z for the 4×4 lattice. We included the anisotropy term in the Hamiltonian as

$$H = J_1 \sum_{\langle \mathbf{r}_i, \mathbf{r}_j \rangle} \mathbf{S}_{\mathbf{r}_i} \cdot \mathbf{S}_{\mathbf{r}_j} + J_2 \sum_{\langle\langle \mathbf{r}_i, \mathbf{r}_j \rangle\rangle} \mathbf{S}_{\mathbf{r}_i} \cdot \mathbf{S}_{\mathbf{r}_j} + J_3 \sum_{\langle\langle\langle \mathbf{r}_i, \mathbf{r}_j \rangle\rangle\rangle} \mathbf{S}_{\mathbf{r}_i} \cdot \mathbf{S}_{\mathbf{r}_j} + \mathbf{B} \cdot \sum_{\mathbf{r}_i} \mathbf{S}_{\mathbf{r}_i} + J_z \sum_{\langle \mathbf{r}_i, \mathbf{r}_j \rangle} S^Z_{\mathbf{r}_i} \cdot S^Z_{\mathbf{r}_j}. \tag{B1}$$

The NN is trained to predict the anisotropy strength J_z, chosen in the interval $[-0.2, 0.2]$, by use of the dynamical correlator $D(\omega)$ as input. The mean error Δ is 0.014. These results show our machine-learning algorithm can be extended to account for anisotropic exchange terms in a spin Hamiltonian.

[1] L. Savary and L. Balents, Quantum spin liquids: A review, Rep. Progr. Phys. **80**, 016502 (2016).
[2] M. R. Norman, Colloquium: Herbertsmithite and the search for the quantum spin liquid, Rev. Mod. Phys. **88**, 041002 (2016).

[3] A. Banerjee, J. Yan, J. Knolle, C. A. Bridges, M. B. Stone, M. D. Lumsden, D. G. Mandrus, D. A. Tennant, R. Moessner, and S. E. Nagler, Neutron scattering in the proximate quantum spin liquid α-$RuCl_3$, Science **356**, 1055 (2017).

[4] C. Broholm, R. J. Cava, S. A. Kivelson, D. G. Nocera, M. R. Norman, and T. Senthil, Quantum spin liquids, Science **367**, eaay0668 (2020).

[5] B. Gao, *et al.*, Experimental signatures of a three-dimensional quantum spin liquid in effective spin-1/2 $Ce_2Zr_2O_7$ pyrochlore, Nat. Phys. **15**, 1052 (2019).

[6] L. Ding, P. Manuel, S. Bachus, F. Grußler, P. Gegenwart, J. Singleton, R. D. Johnson, H. C. Walker, D. T. Adroja, A. D. Hillier, and A. A. Tsirlin, Gapless spin-liquid state in the structurally disorder-free triangular antiferromagnet $NaYbO_2$, Phys. Rev. B **100**, 144432 (2019).

[7] D.-J. Choi, N. Lorente, J. Wiebe, K. von Bergmann, A. F. Otte, and A. J. Heinrich, Colloquium: Atomic spin chains on surfaces, Rev. Mod. Phys. **91**, 041001 (2019).

[8] K. Yang, S.-H. Phark, Y. Bae, T. Esat, P. Willke, A. Ardavan, A. J. Heinrich, and C. P. Lutz, Probing resonating valence bond states in artificial quantum magnets, Nat. Commun. **12**, 993 (2021).

[9] D. M. Eigler and E. K. Schweizer, Positioning single atoms with a scanning tunnelling microscope, Nature **344**, 524 (1990).

[10] C. F. Hirjibehedin, C. P. Lutz, and A. J. Heinrich, Spin coupling in engineered atomic structures, Science **312**, 1021 (2006).

[11] S. Loth, S. Baumann, C. P. Lutz, D. M. Eigler, and A. J. Heinrich, Bistability in atomic-scale antiferromagnets, Science **335**, 196 (2012).

[12] A. A. Khajetoorians, B. Baxevanis, C. Hübner, T. Schlenk, S. Krause, T. O. Wehling, S. Lounis, A. Lichtenstein, D. Pfannkuche, J. Wiebe, and R. Wiesendanger, Current-driven spin dynamics of artificially constructed quantum magnets, Science **339**, 55 (2013).

[13] A. A. Khajetoorians, D. Wegner, A. F. Otte, and I. Swart, Creating designer quantum states of matter atom-by-atom, Nat. Rev. Phys. **1**, 703 (2019).

[14] I.-J. Chen, M. Aapro, A. Kipnis, A. Ilin, P. Liljeroth, and A. S. Foster, Precise atom manipulation through deep reinforcement learning, Nat. Commun. **13**, 7499 (2022).

[15] A. J. Heinrich, J. A. Gupta, C. P. Lutz, and D. M. Eigler, Single-atom spin-flip spectroscopy, Science **306**, 466 (2004).

[16] J. Fernández-Rossier, Theory of Single-Spin Inelastic Tunneling Spectroscopy, Phys. Rev. Lett. **102**, 256802 (2009).

[17] A. Spinelli, B. Bryant, F. Delgado, J. Fernández-Rossier, and A. F. Otte, Imaging of spin waves in atomically designed nanomagnets, Nat. Mater. **13**, 782 (2014).

[18] F. D. Natterer, K. Yang, W. Paul, P. Willke, T. Choi, T. Greber, A. J. Heinrich, and C. P. Lutz, Reading and writing single-atom magnets, Nature **543**, 226 (2017).

[19] K. Yang, W. Paul, S.-H. Phark, P. Willke, Y. Bae, T. Choi, T. Esat, A. Ardavan, A. J. Heinrich, and C. P. Lutz, Coherent spin manipulation of individual atoms on a surface, Science **366**, 509 (2019).

[20] P. Willke, K. Yang, Y. Bae, A. J. Heinrich, and C. P. Lutz, Magnetic resonance imaging of single atoms on a surface, Nat. Phys. **15**, 1005 (2019).

[21] K. Yang, P. Willke, Y. Bae, A. Ferrón, J. L. Lado, A. Ardavan, J. Fernández-Rossier, A. J. Heinrich, and C. P. Lutz, Electrically controlled nuclear polarization of individual atoms, Nat. Nanotechnol. **13**, 1120 (2018).

[22] Y. Chen, Y. Bae, and A. J. Heinrich, Harnessing the quantum behavior of spins on surfaces, Adv. Mater. **35** (2023).

[23] M. F. Crommie, C. P. Lutz, and D. M. Eigler, Confinement of electrons to quantum corrals on a metal surface, Science **262**, 218 (1993).

[24] J. Girovsky, J. L. Lado, F. E. Kalff, E. Fahrenfort, L. J. J. M. Peters, J. Fernández-Rossier, and A. F. Otte, Emergence of quasiparticle Bloch states in artificial crystals crafted atom-by-atom, SciPost Phys. **2**, 020 (2017).

[25] A. A. Khajetoorians, D. Wegner, A. F. Otte, and I. Swart, Creating designer quantum states of matter atom-by-atom, Nat. Rev. Phys. **1**, 703 (2019).

[26] S. E. Freeney, S. T. P. B. andJacob W. Harteveld, and I. Swart, Coupling quantum corrals to form artificial molecules, SciPost Phys. **9**, 085 (2020).

[27] M. N. Huda, S. Kezilebieke, T. Ojanen, R. Drost, and P. Liljeroth, Tuneable topological domain wall states in engineered atomic chains, npj Quantum Mater. **5**, 17 (2020).

[28] N. Nilius, T. M. Wallis, and W. Ho, Development of one-dimensional band structure in artificial gold chains, Science **297**, 1853 (2002).

[29] K. K. Gomes, W. Mar, W. Ko, F. Guinea, and H. C. Manoharan, Designer Dirac fermions and topological phases in molecular graphene, Nature **483**, 306 (2012).

[30] M. N. Huda, S. Kezilebieke, and P. Liljeroth, Designer flat bands in quasi-one-dimensional atomic lattices, Phys. Rev. Res. **2**, 043426 (2020).

[31] Y. Pennec, W. Auwärter, A. Schiffrin, A. Weber-Bargioni, A. Riemann, and J. V. Barth, Supramolecular gratings for tuneable confinement of electrons on metal surfaces, Nat. Nanotechnol. **2**, 99 (2007).

[32] L. Yan and P. Liljeroth, Engineered electronic states in atomically precise artificial lattices and graphene nanoribbons, Adv. Phys. X **4**, 1651672 (2019).

[33] M. R. Slot, T. S. Gardenier, P. H. Jacobse, G. C. P. van Miert, S. N. Kempkes, S. J. M. Zevenhuizen, C. M. Smith, D. Vanmaekelbergh, and I. Swart, Experimental realization and characterization of an electronic Lieb lattice, Nat. Phys. **13**, 672 (2017).

[34] J. Lobo-Checa, M. Matena, K. Müller, J. H. Dil, F. Meier, L. H. Gade, T. A. Jung, and M. Stöhr, Band formation from coupled quantum dots formed by a nanoporous network on a copper surface, Science **325**, 300 (2009).

[35] Y. del Castillo and J. Fernández-Rossier, Certifying entanglement of spins on surfaces using ESR-STM, ArXiv:2211.14205 (2022).

[36] J. Wang, S. Paesani, R. Santagati, S. Knauer, A. A. Gentile, N. Wiebe, M. Petruzzella, J. L. O'Brien, J. G. Rarity, A. Laing, and M. G. Thompson, Experimental quantum Hamiltonian learning, Nat. Phys. **13**, 551 (2017).

[37] E. Bairey, I. Arad, and N. H. Lindner, Learning a local Hamiltonian from Local Measurements, Phys. Rev. Lett. **122**, 020504 (2019).

[38] A. Anshu, S. Arunachalam, T. Kuwahara, and M. Soleimanifar, Sample-efficient learning of interacting quantum systems, Nat. Phys. **17**, 931 (2021).

[39] A. Valenti, E. van Nieuwenburg, S. Huber, and E. Greplova, Hamiltonian learning for quantum error correction, Phys. Rev. Res. **1**, 033092 (2019).

[40] R. Koch and J. L. Lado, Designing quantum many-body matter with conditional generative adversarial networks, Phys. Rev. Res. **4**, 033223 (2022).

[41] A. A. Gentile, B. Flynn, S. Knauer, N. Wiebe, S. Paesani, C. E. Granade, J. G. Rarity, R. Santagati, and A. Laing, Learning models of quantum systems from experiments, Nat. Phys. **17**, 837 (2021).

[42] T. S. Seifert, S. Kovarik, D. M. Juraschek, N. A. Spaldin, P. Gambardella, and S. Stepanow, Longitudinal and transverse electron paramagnetic resonance in a scanning tunneling microscope, Sci. Adv. **6**, eabc5511 (2020).

[43] J. Kim, W.-J. Jang, T. H. Bui, D.-J. Choi, C. Wolf, F. Delgado, Y. Chen, D. Krylov, S. Lee, S. Yoon, C. P. Lutz, A. J. Heinrich, and Y. Bae, Spin resonance amplitude and frequency of a single atom on a surface in a vector magnetic field, Phys. Rev. B **104**, 174408 (2021).

[44] We have considered here the minimal spin Hamiltonian that realizes a frustrated magnet, which is the subject of our study. However, additional terms could be included in this Hamiltonian to study other magnetic phases. For instance, the effect of the Dzyaloshinsky-Moriya interaction has been analyzed within this bottom-up approach [65].

[45] A. W. Sandvik, Evidence for Deconfined Quantum Criticality in a Two-Dimensional Heisenberg Model with Four-Spin Interactions, Phys. Rev. Lett. **98**, 227202 (2007).

[46] L. Capriotti and S. Sachdev, Low-Temperature Broken-Symmetry Phases of Spiral Antiferromagnets, Phys. Rev. Lett. **93**, 257206 (2004).

[47] L. Capriotti, D. J. Scalapino, and S. R. White, Spin-Liquid versus Dimerized Ground States in a Frustrated Heisenberg Antiferromagnet, Phys. Rev. Lett. **93**, 177004 (2004).

[48] W.-Y. Liu, J. Hasik, S.-S. Gong, D. Poilblanc, W.-Q. Chen, and Z.-C. Gu, Emergence of Gapless Quantum Spin Liquid from Deconfined Quantum Critical Point, Phys. Rev. X **12**, 031039 (2022).

[49] K. Choo, T. Neupert, and G. Carleo, Two-dimensional frustrated $J_1 - J_2$ model studied with neural network quantum states, Phys. Rev. B **100**, 125124 (2019).

[50] K. Yang, Y. Bae, W. Paul, F. D. Natterer, P. Willke, J. L. Lado, A. Ferrón, T. Choi, J. Fernández-Rossier, A. J. Heinrich, and C. P. Lutz, Engineering the Eigenstates of Coupled spin-1/2 Atoms on a Surface, Phys. Rev. Lett. **119**, 227206 (2017).

[51] P. Willke, Y. Bae, K. Yang, J. L. Lado, A. Ferrón, T. Choi, A. Ardavan, J. Fernández-Rossier, A. J. Heinrich, and C. P. Lutz, Hyperfine interaction of individual atoms on a surface, Science **362**, 336 (2018).

[52] S. Shehada, M. dos Santos Dias, M. Abusaa, and S. Lounis, Interplay of magnetic states and hyperfine fields of iron dimers on MgO(001), J. Phys.: Condens. Matter **34**, 385802 (2022).

[53] S. Tosoni and G. Pacchioni, Magnetic nature and hyperfine interactions of transition metal atoms adsorbed on ultrathin insulating films: A challenge for DFT, Phys. Chem. Chem. Phys. **24**, 15891 (2022).

[54] ITensor Library, http://itensor.org.

[55] M. Fishman, S. R. White, and E. M. Stoudenmire, The ITensor software library for tensor network calculations, SciPost Phys. Codebases, 4 (2022).

[56] DMRGpy library, https://github.com/joselado/dmrgpy.

[57] A. J. Heinrich, J. A. Gupta, C. P. Lutz, and D. M. Eigler, Single-atom spin-flip spectroscopy, Science **306**, 466 (2004).

[58] S. Baumann, W. Paul, T. Choi, C. P. Lutz, A. Ardavan, and A. J. Heinrich, Electron paramagnetic resonance of individual atoms on a surface, Science **350**, 417 (2015).

[59] The spatial profile in the lattice model is accounted for by a Gaussian envelope of width r_0 $\tilde{\mathcal{S}}(\omega, \mathbf{r}) = \sum_i \mathcal{S}(\omega, \mathbf{r}_i) e^{-|\mathbf{r}-\mathbf{r}_i|^2/2r_0}$.

[60] A. Singha, P. Willke, T. Bilgeri, X. Zhang, H. Brune, F. Donati, A. J. Heinrich, and T. Choi, Engineering atomic-scale magnetic fields by dysprosium single atom magnets, Nat Commun **12**, 4179 (2021).

[61] S. Morita, R. Kaneko, and M. Imada, Quantum spin liquid in spin 1/2 J_1–J_2 Heisenberg model on square lattice: Many-variable variational Monte Carlo study combined with quantum-number projections, J. Phys. Soc. Jpn. **84**, 024720 (2015).

[62] T. Choi, W. Paul, S. Rolf-Pissarczyk, A. J. Macdonald, F. D. Natterer, K. Yang, P. Willke, C. P. Lutz, and A. J. Heinrich, Atomic-scale sensing of the magnetic dipolar field from single atoms, Nat. Nanotechnol. **12**, 420 (2017).

[63] A. Ferrón, S. A. Rodríguez, S. S. Gómez, J. L. Lado, and J. Fernández-Rossier, Single spin resonance driven by electric modulation of the g-factor anisotropy, Phys. Rev. Res. **1**, 033185 (2019).

[64] I.-J. Chen, M. Aapro, A. Kipnis, A. Ilin, P. Liljeroth, and A. S. Foster, Precise atom manipulation through deep reinforcement learning, Nat. Commun. **13**, 7499 (2022).

[65] M. Steinbrecher, R. Rausch, K. T. That, J. Hermenau, A. A. Khajetoorians, M. Potthoff, R. Wiesendanger, and J. Wiebe, Non-collinear spin states in bottom-up fabricated atomic chains, Nat. Commun. **9**, 2853 (2018).